appliedoptics

Accurate feature detection for out-of-focus camera calibration

Yuwei Wang,[1] Xiangcheng Chen,[2,4] Jiayuan Tao,[1] Keyi Wang,[1,5] and Mengchao Ma[3]

[1]*Department of Precision Machinery and Precision Instrumentation, University of Science and Technology of China, Hefei 230026, China*
[2]*School of Automation, Wuhan University of Technology, Wuhan 430070, China*
[3]*Department of Instrument Science and Opto-electronics Engineering, Hefei University of Technology, Hefei 230088, China*
[4]*e-mail: chenxgcg@ustc.edu*
[5]*e-mail: kywang@ustc.edu.cn*

For conventional camera calibration methods, well-focused images are necessary to detect features accurately. However, this requirement causes practical inconveniences to image acquisition for long- and short-distance photogrammetry. In this study, three active phase-shift circular grating (PCG) arrays are used as calibration patterns. The PCGs' centers are regarded as feature points that can be accurately extracted by ellipse fitting of 2π-phase points even though patterns are substantially blurred. In the experiments, Gaussian filters are utilized to blur pattern images, and different standard deviations are set for different fuzzy degrees. Pattern images with different defocusing degrees are also captured. The period and number of PCGs and noise are considered. Experimental results indicate that our method is accurate, reliable, and insensitive to image defocusing.   © 2016 Optical Society of America

1. INTRODUCTION

Camera calibration is essential for imaging-based optical metrology to establish the mapping between world points and their image projections. The calibration result is highly depended on the precision of feature detection. Two calibration methods, namely, metric and self-calibration, are commonly used [1–3]. In metric calibration, a calibration target with exactly known feature points is observed. In self-calibration, feature points in a scene are used. More efficient results are computed by using metric calibration than by using self-calibration.

Calibration targets, such as planar boards, are commonly utilized in metric calibration. Planar boards are usually marked by two types of patterns: checkerboards [2–4] and circles [5–8]. For these planar target-based calibration methods, well-focused images are necessary to detect features accurately [9] because an out-of-focus calibration target results in a defocused image, which negatively influences gray-based feature detection. This drawback also causes practical inconveniences to calibration image acquisition, especially for long- (Fig. 1) and short-distance photogrammetry (Fig. 2) [10,11]. For example, calibration targets should be very small if cameras are set to focus at a very short distance. Conversely, targets should be large enough to cover a sufficient field of view if cameras are set to focus over a long distance. Therefore, several camera calibration methods have been proposed to allow placing out-of-focus calibration targets. For instance, feature points are extracted from five complementary binary patterns on the basis of the defocus blur modeled as a convolution of a sharp image with a Gaussian point spread function [9]. Blurred edges likely satisfy certain intensity functions [12]. Some phase patterns have been used as calibration patterns tolerant against image defocusing. Thus, targets do not need to be in focus. Three- and four-step phase-shift fringe patterns have been utilized to generate correspondences between world and image points [13,14]. Horizontal and vertical phase distributions of a crossed fringe pattern have been calculated with the Fourier transform method, and each pixel with a valid phase can be regarded as a feature point in the calibration [15]. The feature detection of active sinusoidal fringe patterns has been enhanced through "virtual defocusing" and windowed polynomial fitting, and an accuracy of 0.0067 pixels has been obtained [16]. Zero-phase intersection points have been extracted from concentric circles and wedge gratings, and orthogonal vanishing points have been calculated to calibrate cameras [17]. These active patterns are usually displayed on monitors, tablets, or smartphones with the advantages of guaranteed flatness and known pixel sizes. Arbitrary planar patterns can be obtained through simple programming, which entails low cost and requires minimum
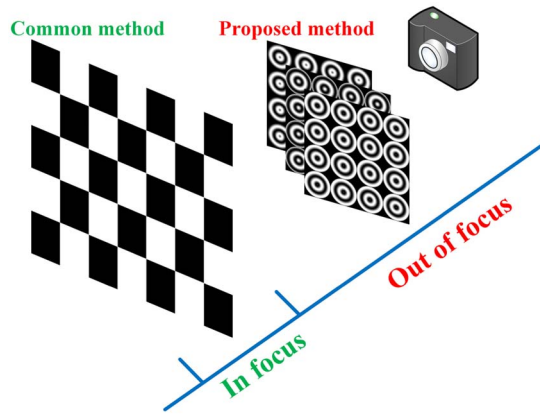
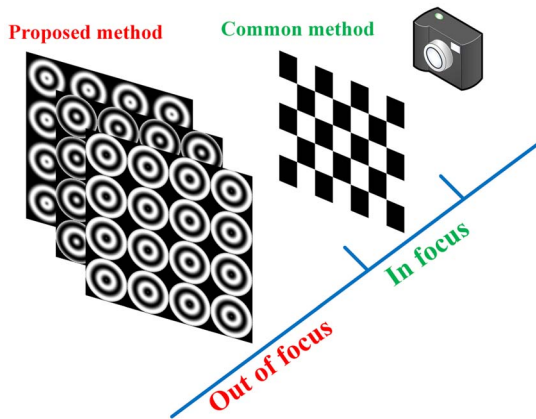**Fig. 1.**   Long-distance photogrammetry.

Fig. 2.   Short-distance photogrammetry.

effort. It also enables accurate and precise feature detection because of advanced fringe analysis [16]. However, previous studies mainly investigated feature detection and accuracy improvement with well-focused images.

In this study, phase-shift circular grating (PCG) arrays were used to create robust calibration patterns for image defocusing. The patterns can be displayed conveniently on a planar liquid crystal display (LCD) monitor that enables cameras to capture images at the same viewpoint. The PCGs' centers were regarded as feature points and extracted by ellipse fitting of 2π-phase points. In the experiments, Gaussian filters were utilized to blur well-focused images, and different standard deviations were set for different fuzzy degrees. Gaussian white noises were added to the pattern images to test the noise immunity of our method. Two other groups of pattern images were also captured out-of-focus to obtain different defocusing degrees. The period and number of PCGs were also considered. Experimental results indicated that the proposed method is accurate, reliable, and insensitive to image defocusing.

This paper is organized as follows. Section 2 describes our camera model, PCG arrays, and feature detection method. Section 3 discusses our experiments to test the proposed method. Section 4 presents our conclusions.

2. CAMERA CALIBRATION METHOD

A. Camera Model

An ordinary pinhole camera model was used [18], as shown in Fig. 3. Let us denote the augmented vector of a 3D world point by using $P = (x, y, z, 1)^T$ and a 2D image point by using $p = (u, v, 1)^T$. The relationship between P and p is given by the equation

$$\lambda p = K[R \quad t]P \quad \text{with } K = \begin{bmatrix} f_u & \gamma & u_0 \\ 0 & f_v & v_0 \\ 0 & 0 & 1 \end{bmatrix}, \quad (1)$$

where λ is an arbitrary scale factor. The 3×3 matrix K containing the focal length (f_u, f_v), principal point (u_0, v_0), and skew angle parameter γ denotes the camera intrinsic matrix. $[R \quad t]$, called the extrinsic parameter, is a 3×4 matrix representing rotation and translation that relates the world coordinates to the camera coordinates. In general, distortions should be considered to achieve a higher accuracy [18]. Therefore, intrinsic and extrinsic parameters can be calibrated by solving Eq. (1) if the one-to-one mapping between world points P and image points p is obtained [2].

B. Phase-shift Circular Grating (PCG)

Phase-shift methods are widely used in 3D shape measurements because of their speed and accuracy [19–22]. The calibration targets used in this study are marked by three PCG arrays with a phase shift of $2\pi/3$. The intensities of the three PCG arrays can be described as [17]

$$\begin{cases} I_1(x, y) = A + B \cos[\phi(x, y) - 2\pi/3], \\ I_2(x, y) = A + B \cos[\phi(x, y)], \\ I_3(x, y) = A + B \cos[\phi(x, y) + 2\pi/3], \end{cases} \quad (2)$$

where A and B are constants ($A = 0.5$, $B = 0.5$) and $\phi(x, y)$ is the unwrapped phase, which can be described by

$$\phi(x, y) = \frac{2\pi r(x, y)}{T}, \quad (3)$$

where constant T denotes the period of the PCG; radius $r(x, y)$ is the Euclidean distance between points (x, y) of the PCG and its center (x_0, y_0), which is given by Eq. (4):
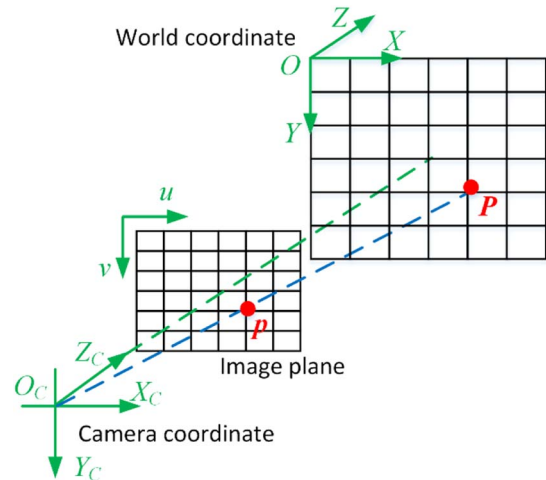

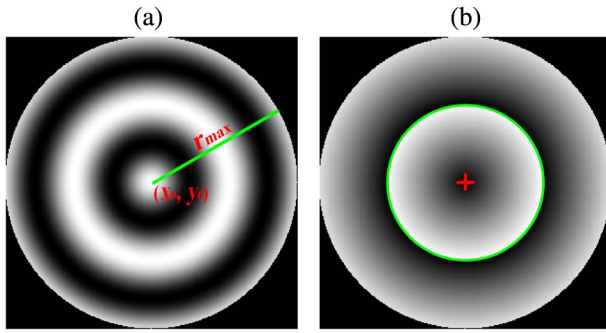
Fig. 3.   Pinhole camera model.

Fig. 4. PCG pattern. (a) A PCG, and (b) its wrapped phase.

$$r(x, y) = \sqrt{(x - x_0)^2 + (y - y_0)^2}. \qquad (4)$$

Equation (4) indicates that points (x, y) distributed on a circle yield the same $\phi(x, y)$; in turn, points with the same $\phi(x, y)$ have the same $r(x, y)$. In special cases, the PCG's center with $r(x_0, y_0) = 0$ exhibits the minimum phase $\phi(x_0, y_0) = 0$. In Fig. 4, the 2π-phase points are distributed on a circle with $r(x, y) = T$. r_{max} is the maximum value of $r(x, y)$, which must be greater than T to ensure a complete PCG period; therefore, we usually set $1.2T \leq r_{max} < 2T$.

However, a PCG only contains one center. Therefore, we need PCG arrays to gain multiple circle centers as feature points. For PCG arrays with $M \times N$ uniform PCGs, the center (x_0^k, y_0^k) of the mth row and nth column PCG is set as

$$\begin{cases} x_0^k = r_{max} + (n - 1)DH, \\ y_0^k = r_{max} + (m - 1)DV, \end{cases} \text{with } k = (m, n), \qquad (5)$$

where $m = 0, 1, \ldots, M - 1$ and $n = 0, 1, \ldots, N - 1$; DH and DV are the spaces between adjacent centers along the horizontal and vertical directions, and their values are equal and known. We commonly set $DH = DV \geq 2r_{max}$ to avoid interference between adjacent PCGs. These PCG array patterns can be generated by a simple computer program and displayed conveniently on a LCD monitor controlled by a computer. Figure 5 shows a 3×3 PCG array and its wrapped phase in which green circles express the 2π-phase points and the red points are their centers used for camera calibration.
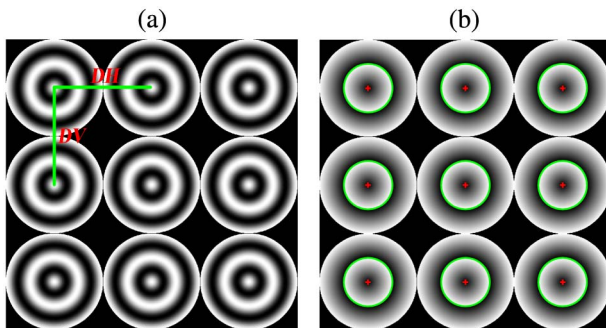

Fig. 5. PCG array pattern. (a) A PCG array, and (b) its wrapped phase.

C. Feature Detection

Once the three PCG array images are captured by the camera for calibration, the phase $\varphi(u, v)$ can be calculated on the basis of the three-step phase-shifting algorithm [19]

$$\varphi(u, v) = \arctan\left(\sqrt{3}\,\frac{J_1 - J_3}{2J_2 - J_1 - J_3}\right), \qquad (6)$$

where $J_i(u, v)(i = 1, 2, 3)$ represents the three PCG array images, and (u, v) denotes the image point. Figure 6(a) shows the sample image $J_2(u, v)$. The wrapped phase distributions range from 0 to 2π, with 2π discontinuities, because of the nature of the arctangent function. 2π-phase detection receives the highest precision [17]; the imaged 2π-phase points are distributed on an ellipse or a circle in special cases [23]. We can utilize an ellipse-fitting technique to extract the imaged centers of the PCGs. Let us represent a general ellipse curve in the following manner:

$$au^2 + buv + cv^2 + du + ev + f = 0. \qquad (7)$$

The ellipse center (u_0^e, v_0^e), which is approximately considered as the imaged center of the circle [18], can be obtained by using the following equations:

$$u_0^e = \frac{2cd - be}{b^2 - 4ac} \quad \text{and} \quad v_0^e = \frac{2ae - bd}{b^2 - 4ac}. \qquad (8)$$

The key step is 2π-phase point detection that directly determines the ellipse curve and its center point. However, the phase-shift algorithm can achieve pixel-level accuracy. Therefore, 2π-phase points should be optimized to reach subpixel accuracy. The feature detection is detailed below.

Step 1: Phase-modulated areas can be obtained using Eq. (9) because of a large gray difference between the background and the phase-modulated areas
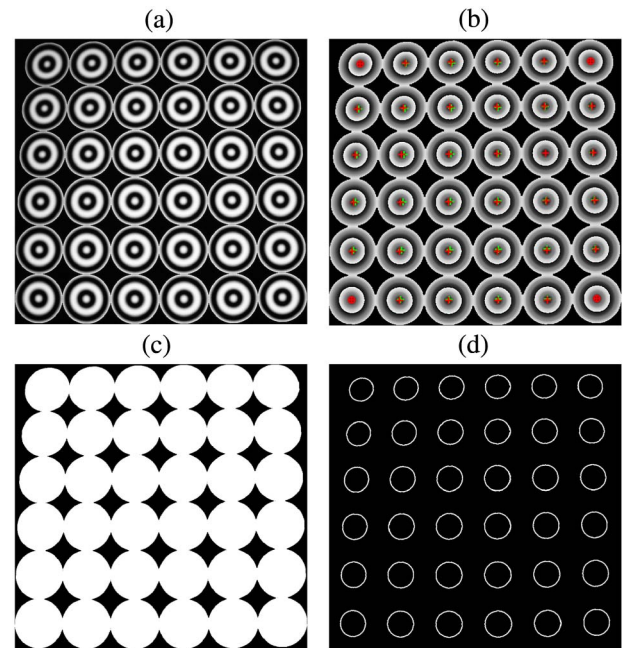

Fig. 6. Feature detection example. (a) PCG array images, (b) wrapped phase image, (c) phase-modulated areas (white), and (d) rough 2π-phase points.

$$Area = \begin{cases} 1, & \text{if } (J_1 + J_2 + J_3) > \text{threshold}, \\ 0, & \text{otherwise.} \end{cases} \quad \textbf{(9)}$$

Morphological erosion and dilation methods [24] are also applied to eliminate the discrete noise points and holes. Erosion and dilation with a structuring element SE are expressed as

$$\begin{cases} \text{imerode}(Area, SE) = \{x : SE_x \subset Area\}, \\ \text{imdilate}(Area, SE) = \cup\{SE_x : x \in Area\}, \end{cases} \quad \textbf{(10)}$$

where subscripted SE_x denotes the translation of the origin of SE to the point x within $Area$. Figure 6(c) shows the segmentation result with a gray threshold of 50, and the structuring elements SE used for erosion and dilation (with *"imerode"* and *"imdilate"* in MATLAB) are 3×3 and 5×5 matrices of ones, respectively.

Step 2: On the basis of Eq. (6), we can acquire the wrapped phase of the PCG array images, as shown in Fig. 6(b). Referring to the well-known Camera Calibration Toolbox for MATLAB [25], a user can interactively specify the four extreme PCG centers of the wrapped phase image and find these centers by returning the minimum-phase points (red circle "o") within the search window centered on the user-selected points. A grid (green cross "+") can be built on the basis of known PCG numbers $M \times N$ along the horizontal and vertical directions and the spaces DH and DV by using planar collineation in the absence of distortion. For each point of the grid, we find the minimum-phase point (u_0^k, v_0^k) (red cross "+") within its neighborhood, which can be regarded as the rough locations of the imaged PCG centers.

Step 3: The wrapped phase experiences abrupt changes at 2π-phase points because of 2π discontinuities. Therefore, we can detect the 2π-phase points via the conventional Sobel edge-detection algorithm [26]. The detected edges (with *"edge"* in MATLAB) are shown in Fig. 6(d). If an edge point is nearest to (u_0^k, v_0^k) among the imaged centers of the PCGs, the edge point possibly belongs to the kth PCG. Thus, the rough 2π-phase points (u_i^k, v_i^k) of the kth *PCG* can be determined.

Step 4: For each (u_i^k, v_i^k), its neighborhood points (u_{ij}^k, v_{ij}^k) with the wrapped phase $\varphi(u_{ij}^k, v_{ij}^k)$ are selected (Fig. 7). The unwrapped phase can be calculated by using the following equation:
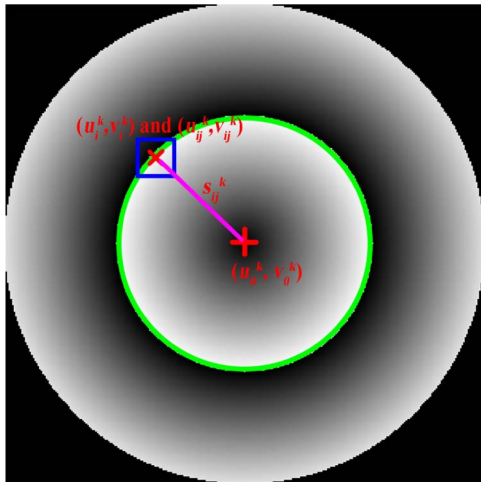

Fig. 7. 2π-phase point optimization.

$$\varphi'(u_{ij}^k, v_{ij}^k) = \begin{cases} \varphi(u_{ij}^k, v_{ij}^k) & \varphi(u_{ij}^k, v_{ij}^k) \geq \pi, \\ \varphi(u_{ij}^k, v_{ij}^k) + 2\pi & \varphi(u_{ij}^k, v_{ij}^k) < \pi. \end{cases} \quad \textbf{(11)}$$

The Euclidean distance between (u_0^k, v_0^k) and (u_{ij}^k, v_{ij}^k) can be written as follows:

$$s_{ij}^k = \sqrt{(u_{ij}^k - u_0^k)^2 + (v_{ij}^k - v_0^k)^2}. \quad \textbf{(12)}$$

According to Eq. (3), $\phi(x, y)$ and $r(x, y)$ exhibit a linear relationship. Therefore, we assumed that a linear relationship also exists between $\varphi'(u_{ij}^k, v_{ij}^k)$ and s_{ij}^k within a small area. Thus, we used a least-squares linear-fitting algorithm (with *"polyfit"* in MATLAB) to establish the relations $s = f(\varphi')$, with s_{ij}^k and $\varphi'(u_{ij}^k, v_{ij}^k)$ as inputs. Moreover, we limit the desired 2π-phase point (p_i^k, q_i^k) on the straight line defined by (u_i^k, v_i^k) and (u_0^k, v_0^k). The optimized 2π-phase point (p_i^k, q_i^k) with subpixel accuracy can be calculated with the following equations:

$$\begin{cases} f(2\pi) = \sqrt{(p_i^k - u_0^k)^2 + (q_i^k - v_0^k)^2}, \\ (u_i^k - u_0^k)(q_i^k - v_0^k) = (v_i^k - v_0^k)(p_i^k - u_0^k). \end{cases} \quad \textbf{(13)}$$

Step 5: After the refined 2π-phase points (p_i^k, q_i^k) of the kth PCG are obtained, a least-squares ellipse-fitting algorithm [27] is employed to compute the ellipse curve and its center point. Using the one-to-one mapping between the centers of the PCGs and their projections, we can calibrate the camera.

3. EXPERIMENTS

A camera calibration system comprising a camera, an LCD monitor, and a computer was set up (Fig. 8) to validate the proposed method experimentally. We used a Canon EOS-M2 with a zoom lens. The resolution of the camera is 1920×1280 pixels. The LCD monitor has a resolution of 1920×1080 pixels and a pixel pitch of 0.18 mm. Three PCG arrays were generated and displayed conveniently on the monitor as the camera captured images. The origin of the world reference frame was located in the top-left PCG center, and the Z axis was perpendicular to the planar monitor. Therefore, the feature points had the same $z = 0$. The camera was fixed on a tripod and controlled by a wireless controller to ensure stable image acquisition. All programs were implemented in MATLAB.

Fig. 8. Experimental setup.

Image Processing Toolbox [28] and Camera Calibration Toolbox [25] were used.

The first group of well-focused images was taken from six different viewpoints. Indoor light sources were turned off during image acquisition. The calibration patterns were three PCG arrays containing 6×6 uniform PCGs and a checkerboard with 6×6 corners for the contrast experiment, with a total of 6×6 feature points. The parameters of the PCG arrays were: $A = 0.5$, $B = 0.5$, $T = 40$ pixels, and $DH = DV = 150$ pixels. The square size of the checkerboard was 150×150 pixels. One image of the PCG arrays is shown in Fig. 6(a). Calibration accuracy can be assessed on the basis of the mean re-projection error (MRE) of feature points [9,29]. MRE can be computed by the equation

$$\text{MRE} = \frac{\sum_{l=1}^{L} \sum_{m=1}^{M} \sum_{n=1}^{N} \| p(l, m, n) - q(l, m, n) \|}{LMN}, \quad (14)$$

where L is the total number of frames, $M \times N$ is the total number of the feature points per frame, $p(l, m, n)$ is the detected feature point, and $q(l, m, n)$ is the re-projection of feature point.

A. Gaussian Blur

We utilized several 25×25 Gaussian filters to blur the pattern images and to compare the performances of the PCG arrays and checkerboard in dealing with fuzzy images. Different standard deviations (from 1 to 20 with a step of 1) were set for different fuzzy degrees (Fig. 9). The MREs of the two methods are shown in Fig. 10. For the original images, the MRE of the PCG array method was approximately 0.08 pixels, which was slightly less than that of the checkerboard method. As the standard deviation increased, the pattern images became more blurred. As a consequence, the MRE of the PCG array method was kept at approximately 0.08 pixels and the MRE of the checkerboard method was significantly increased. The PCG array method exhibits insensitivity to fuzzy images and achieves a higher performance than the checkerboard method.
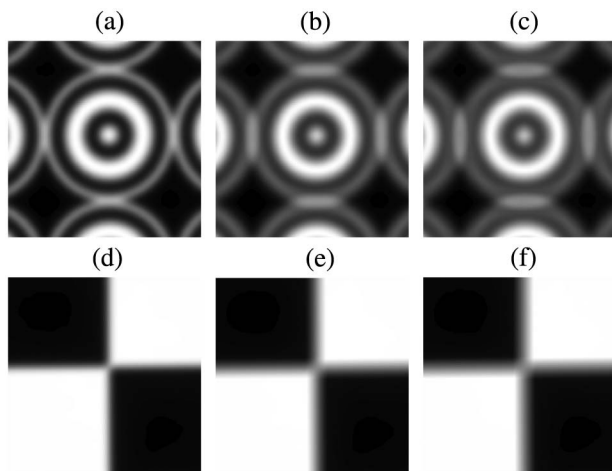

Fig. 10. MREs with Gaussian filters yielding different standard deviations.

B. Gaussian Noise

Noise influences calibration accuracy. Therefore, we added Gaussian white noise with 0 mean and different variances to the pattern images of the first group, as shown in Fig. 11. The variance, which can express the noise level, ranges from 0 to 0.03 with a step of 0.002. In Fig. 12, MREs of the two methods increase nonlinearly with the noise level. However, the mean rate of the checkerboard curve is much larger than that of the PCG array curve. Our method shows a better noise immunity than the checkerboard method.

C. Image Defocusing

Two other groups of pattern images were also captured from six different viewpoints. However, the calibration targets were captured out-of-focus. Thus, we can acquire the pattern images of different defocusing degrees. Figure 13 shows some experimental images from the three groups. The wrapped phase images with the detected feature points (red cross "+") are shown in Fig. 14. The calibration results from the three groups are shown

Fig. 9. Example images with Gaussian filters yielding different standard deviations. (a)–(c) PCG array images: standard deviation = 5, 10, and 20 pixels, respectively; (d)–(f) checkerboard images: standard deviation = 5, 10, and 20 pixels, respectively.
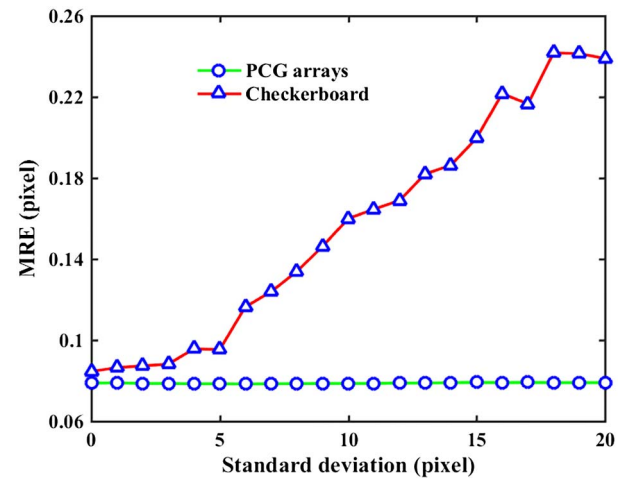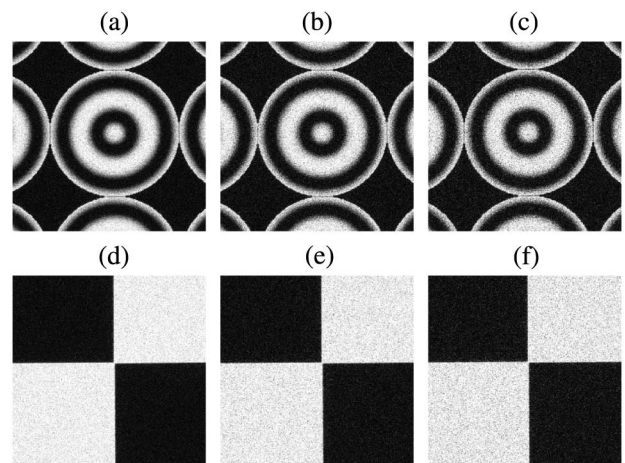

Fig. 11. Example images with Gaussian noises yielding different variances. (a)–(c) PCG array images: variance = 0.01, 0.02, and 0.03, respectively; (d)–(f) checkerboard images: variance = 0.01, 0.02, and 0.03, respectively.
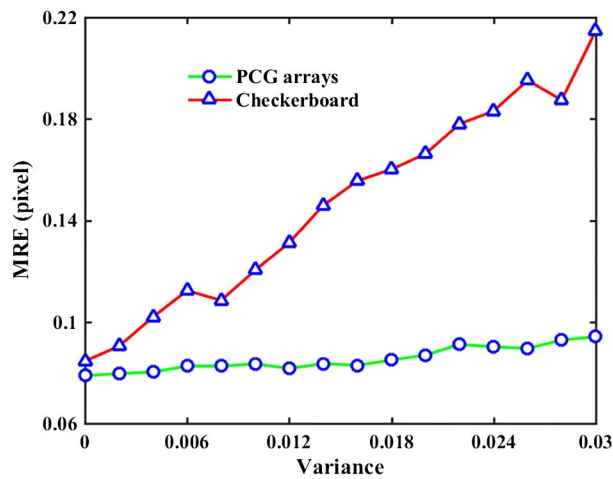
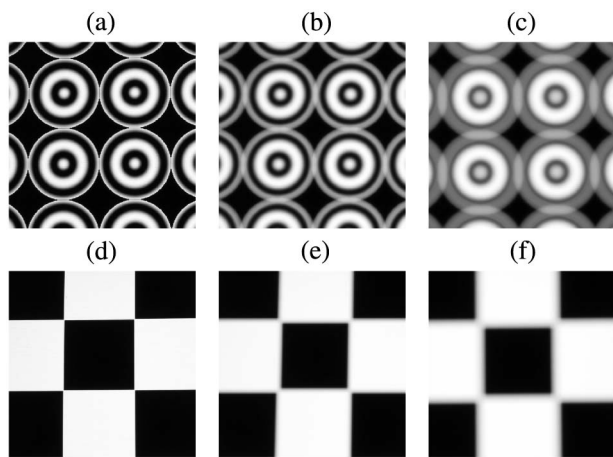**Fig. 12.** MREs with Gaussian noises yielding different variances.

Fig. 13. Calibration images from three groups. (a)–(c) PCG array images from three groups, respectively; (d)–(f) checkerboard images of the three groups, respectively.

in Table 1. The PCG array method can accurately calibrate a camera with defocused images.

D. PCG Period

This experiment investigates the performance of the proposed method in terms of the period of PCGs that corresponds to the radius of 2π-phase circles. We captured five groups of PCG array images from six viewpoints. The PCG arrays contained 5×5 uniform PCGs with $T = 20, 30, 40, 50, 60,$ and 70 pixels. DH and DV are equal to 200 pixels. In Table 2, focal length, principal point, and MRE exhibit slight changes. The maximum differences in f_u, f_v, u_0, and v_0 are less than one pixel. The period of the PCG slightly influences the calibration results within a certain range. If the period is too small, the radius of the 2π-phase circle is also too small to ensure the accuracy of ellipse fitting. If the period is too large, the approximate relation of the ellipse center and the projected center of the PCG is not available, and the monitor should be large enough to display PCG arrays. Therefore, a suitable period is necessary.
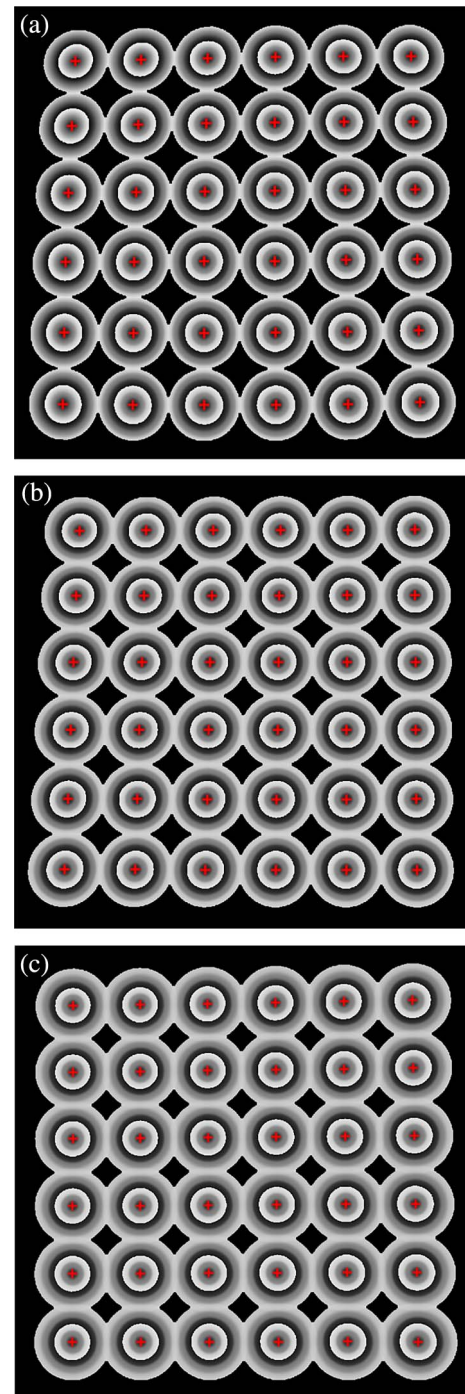

Fig. 14. Wrapped phase images with detected feature points. (a) First group, (b) second group, and (c) third group.

E. Number of PCGs

The number of feature points should also be considered. Therefore, the arrays with 3×3, 4×4, 5×5, 6×6, 7×7, and 8×8 PCGs were captured from six viewpoints and used for the calibration. The periods of all PCGs are equal to 40 pixels. Figure 15 illustrates the MREs with different numbers of PCGs. As the number of PCGs increases, the MRE decreases. Therefore, sufficient feature points are critical for accurate calibration.

Table 1. Calibration Results of the Three Groups (unit: pixel)[a]

Group	Pattern	f_u	f_v	u_0	v_0	MRE
First	PA	1543.5	1543.4	972.1	619.8	**0.0788**
	CB	1543.7	1543.6	971.2	618.6	0.0845
Second	PA	2633.4	2633.2	979.1	597.1	**0.0779**
	CB	2484.8	2483.4	978.4	581.7	1.1080
Third	PA	4543.8	4544.3	993.7	554.3	**0.0755**
	CB	5753.9	5758.2	981.1	572.5	7.2483

[a]PA and CB are the abbreviations of PCG arrays and checkerboard.

Table 2. Calibration Results with Different Periods of PCG (unit: pixel)

T	f_u	f_v	u_0	v_0	MRE
20	1597.8	1597.5	973.3	618.5	**0.0931**
30	1597.9	1597.5	973.3	618.3	**0.0923**
40	1597.6	1597.2	973.4	618.3	**0.0916**
50	1598.0	1597.7	973.4	618.0	**0.0934**
60	1597.8	1597.4	973.3	618.0	**0.0939**
70	1597.6	1597.1	973.4	617.8	**0.0958**
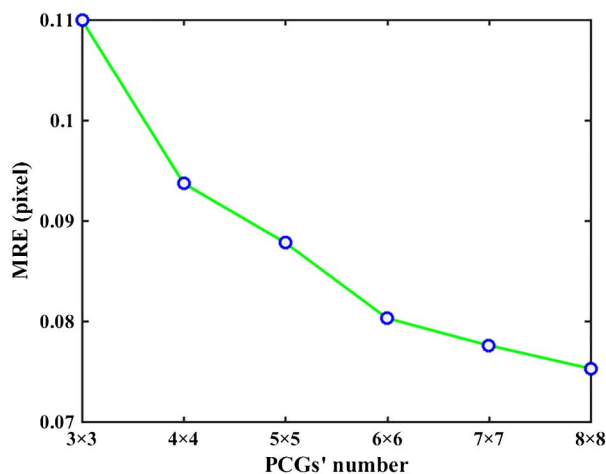
Fig. 15. MREs with different numbers of PCGs.

4. CONCLUSIONS

In this study, three active PCG arrays are used as calibration patterns for accurate camera calibration. The 2π-phase points are detected and refined to obtain subpixel accuracy. The centers of the PCGs are regarded as feature points and extracted by using the ellipse-fitting algorithm. Experimental results indicate that the proposed method is accurate, reliable, and insensitive to image defocusing. Our method also exhibits good noise immunity. Therefore, the proposed method can be used for long- and short-distance photogrammetry and other strict conditions in which traditional calibration targets would be difficult to be placed in focus.

REFERENCES

1. R. Juarez-Salazar, F. Guerrero-Sanchez, C. Robledo-Sanchez, and J. González-García, "Camera calibration by multiplexed phase encoding of coordinate information," Appl. Opt. **54**, 4895–4906 (2015).
2. Z. Zhang, "A flexible new technique for camera calibration," IEEE Trans. Pattern Anal. Mach. Intell. **22**, 1330–1334 (2000).
3. C. Ricolfe-Viala and A.-J. Sánchez-Salmerón, "Robust metric calibration of non-linear camera lens distortion," Pattern Recognit. **43**, 1688–1699 (2010).
4. Q. Zhang and R. Pless, "Extrinsic calibration of a camera and laser range finder (improves camera calibration)," in *Proceedings IEEE/RSJ International Conference on Intelligent Robots and Systems (IROS)* (IEEE, 2004), pp. 2301–2306.
5. G. Jiang and L. Quan, "Detection of concentric circles for camera calibration," in *IEEE International Conference on Computer Vision (ICCV)* (IEEE, 2005), pp. 333–340.
6. J.-S. Kim, H.-W. Kim, and I. S. Kweon, "A camera calibration method using concentric circles for vision applications," *Asian Conference on Computer Vision*, Melbourne, Australia, 2002.
7. X. Chen, Y. Hu, Z. Ma, S. Yu, and Y. Chen, "The location and identification of concentric circles in automatic camera calibration," Opt. Laser Technol. **54**, 185–190 (2013).
8. S. Daftry, M. Maurer, A. Wendel, and H. Bischof, "Flexible and user-centric camera calibration using planar fiducial markers," in *British Machine Vision Conference* (CiteSeerX, 2013).
9. H. Ha, Y. Bok, K. Joo, J. Jung, and I. So Kweon, "Accurate camera calibration robust to defocus using a smartphone," in *Proceedings of the IEEE International Conference on Computer Vision* (2015), pp. 828–836.
10. H. Kauhanen, N. Heiska, and M. Kurkela, "Long focal length imaging for photogrammetric reconstruction," in *International Archives of the Photogrammetry, Remote Sensing and Spatial Information Sciences* (CiteSeerX, 2009), pp. 1682–1750.
11. C. Stamatopoulos and C. S. Fraser, "Calibration of long focal length cameras in close range photogrammetry," Photogrammetric Rec. **26**, 339–360 (2011).
12. M. Baba, M. Mukunoki, and N. Asada, "A unified camera calibration using geometry and blur of feature points," in *International Conference on Pattern Recognition (ICPR)* (IEEE, 2006), pp. 816–819.
13. M. Ma, X. Chen, and K. Wang, "Camera calibration by using fringe patterns and 2D phase-difference pulse detection," Optik **125**, 671–674 (2014).
14. C. Schmalz, F. Forster, and E. Angelopoulou, "Camera calibration: active versus passive targets," Opt. Eng. **50**, 113601 (2011).
15. Y. Liu and X. Su, "Camera calibration with planar crossed fringe patterns," Optik **123**, 171–175 (2012).
16. L. Huang, Q. Zhang, and A. Asundi, "Camera calibration with active phase target: improvement on feature detection and optimization," Opt. Lett. **38**, 1446–1448 (2013).
17. J. Xue, X. Su, L. Xiang, and W. Chen, "Using concentric circles and wedge grating for camera calibration," Appl. Opt. **51**, 3811–3816 (2012).
18. J. Heikkila, "Geometric camera calibration using circular control points," IEEE Trans. Pattern Anal. Mach. Intell. **22**, 1066–1077 (2000).
19. P. S. Huang and S. Zhang, "Fast three-step phase-shifting algorithm," Appl. Opt. **45**, 5086–5091 (2006).
20. S. Zhang, "Composite phase-shifting algorithm for absolute phase measurement," Opt. Lasers Eng. **50**, 1538–1541 (2012).
21. M. Gupta and S. K. Nayar, "Micro phase shifting," in *IEEE Conference on Computer Vision and Pattern Recognition (CVPR)* (IEEE, 2012), pp. 813–820.
22. K. Liu, Y. Wang, D. L. Lau, Q. Hao, and L. G. Hassebrook, "Dual-frequency pattern scheme for high-speed 3-D shape measurement," Opt. Express **18**, 5229–5244 (2010).
23. X. Meng and Z. Hu, "A new easy camera calibration technique based on circular points," Pattern Recognit. **36**, 1155–1164 (2003).
24. F. Nellros, M. J. Thurley, H. Jonsson, C. Andersson, and S. P. Forsmo, "Automated measurement of sintering degree in optical

microscopy through image analysis of particle joins," Pattern Recognit. **48**, 3451–3465 (2015).

25. J.-Y. Bouguet, "Camera calibration toolbox for MATLAB," http://www.vision.caltech.edu/bouguetj/calib_doc/index.html.

26. W. Gao, X. Zhang, L. Yang, and H. Liu, "An improved Sobel edge detection," in *IEEE International Conference on Computer Science and Information Technology (ICCSIT)* (IEEE, 2010), pp. 67–71.

27. A. Fitzgibbon, M. Pilu, and R. B. Fisher, "Direct least square fitting of ellipses," IEEE Trans. Pattern Anal. Mach. Intell. **21**, 476–480 (1999).

28. Mathworks, "Image Processing Toolbox," http://www.mathworks.com/help/images/index.html.

29. S. Vidas, R. Lakemond, S. Denman, C. Fookes, S. Sridharan, and T. Wark, "A mask-based approach for the geometric calibration of thermal-infrared cameras," IEEE Trans. Instrum. Meas. **61**, 1625–1635 (2012).